University of Nebraska - Lincoln
DigitalCommons@University of Nebraska - Lincoln

Evgeny Tsymbal Publications | Research Papers in Physics and Astronomy

2020

Insulator-to-conductor transition controlled by the Rashba-Zeeman effect

L. L. Tao and E. Y. Tsymbal

Follow this and additional works at: https://digitalcommons.unl.edu/physicstsymbal

 Part of the Condensed Matter Physics Commons

This Article is brought to you for free and open access by the Research Papers in Physics and Astronomy at DigitalCommons@University of Nebraska - Lincoln. It has been accepted for inclusion in Evgeny Tsymbal Publications by an authorized administrator of DigitalCommons@University of Nebraska - Lincoln.

npj Computational Materials

www.nature.com/npjcompumats

ARTICLE OPEN

Check for updates

Insulator-to-conductor transition driven by the Rashba–Zeeman effect

Lingling Tao[1]✉ and Evgeny Y. Tsymbal[1]✉

The Rashba effect has recently attracted great attention owing to emerging physical properties associated with it. The interplay between the Rashba effect and the Zeeman effect, being produced by the exchange field, is expected to broaden the range of these properties and even result in novel phenomena. Here we predict an insulator-to-conductor transition driven by the Rashba–Zeeman effect. We first illustrate this effect using a general Hamiltonian model and show that the insulator-to-conductor transition can be triggered under certain Rashba and exchange-field strengths. Then, we exemplify this phenomenon by considering an Ag_2Te/Cr_2O_3 heterostructure, where the electronic structure of the Ag_2Te monolayer is affected across the interface by the proximity effect of the Cr_2O_3 antiferromagnetic layer with well-defined surface magnetization. Based on first-principles calculations, we predict that such a system can be driven into either insulating or conducting phase, depending on the surface magnetization orientation of the Cr_2O_3 layer. Our results enrich the Rashba–Zeeman physics and provide useful guidelines for the realization of the insulator-to-conductor transition, which may be interesting for experimental verification.

npj Computational Materials (2020)6:172 ; https://doi.org/10.1038/s41524-020-00441-0

INTRODUCTION

The Rashba effect is a momentum-dependent spin splitting of the energy bands driven by spin-orbit coupling (SOC)[1]. This phenomenon has recently stimulated vigorous research, owing to its potential application in spintronics[2]. The Rashba effect occurs in material systems with broken space-inversion symmetry such as surfaces[3], interfaces[4], and certain bulk materials[5–7]. The SOC effect allows an electrical control of the spin degree of freedom that is interesting for device applications. For example, using the Rashba effect has been proposed for design of a spin field-effect transistor[8]. Electrically switchable SOC parameter has been explored to design valley-spin valves[9] and valley-spin logic gates[10]. Furthermore, various physical phenomena such as current-induced spin polarization[11], the spin Hall effect[12], and the spin galvanic effect[13,14] have been inspired or reinvigorated.

The Rashba-affected material systems may also exhibit a Zeeman effect. The Zeeman effect is characterized by the momentum-independent spin splitting of the energy bands and is associated with the interaction of spin with an external magnetic field or an exchange field. The Zeeman energy is typically ~0.1 meV/T and therefore is relatively small for applied external fields of a few Tesla or less. In contrast, the internal exchange fields arising from intrinsic magnetization[15], doped magnetic transition metals[16] or ferromagnetic (FM)[17], antiferromagnetic (AFM)[18], and multiferroic[19] insulator substrates owing to magnetic proximity effects[20] can be sizable (~10^2–10^3 T) and hence produce a non-negligible Zeeman splitting of the energy bands.

The interplay between the Rashba and Zeeman effects (abbreviated below as the Rashba–Zeeman effect) is expected to produce novel features not found in pure Rashba- or Zeeman-affected systems. For example, broken time-reversal symmetry owing to the exchange field gives rise to the anomalous Hall effect[21]. In addition, magnetically doped Rashba systems demonstrate entanglement of the spin-orbit and magnetic orders. For example, the recent experimental work on Mn-doped GeTe has demonstrated that the Rashba spin helicity can be altered by magnetization switching[22], and conversely, the magnetization can be reversed by polarization switching[23] or by the current-induced spin-orbit torque[24]. Moreover, the Rashba–Zeeman effect can also affect the quantum transport properties. For example, it has been demonstrated that in quantum-point-contact InSb nanowires with sizable Rashba SOC, the measured conductance plateau could be tuned from e^2/h to $2e^2/h$ by the magnetic field orientation[25].

In this work, we predict another striking phenomenon—an insulator-to-conductor transition induced by the Rashba–Zeeman effect in a two-dimensional (2D) system. The band structure of the 2D material can be controlled by the exchange field orientation, and under certain Rashba and exchange field strengths exhibits an insulator-to-conductor transition. We explore this phenomenon for a realistic system—a monolayer of Ag_2Te deposited on an AFM Cr_2O_3 (0001) substrate. Owing to broken inversion symmetry, an Ag_2Te monolayer exhibits a sizable Rashba band splitting, while the Cr_2O_3 substrate has a robust surface magnetization coupled to the AFM order parameter and provides an exchange field affecting the electronic structure of the Ag_2Te through the proximity effect. Based on density-functional theory (DFT) calculations, we demonstrate that such a system can be driven into either insulating or conducting phase, depending on the boundary magnetization orientation of the Cr_2O_3 layer.

RESULTS AND DISCUSSION

Hamiltonian model and phase diagram

We first illustrate the insulator-to-conductor transition using a general Hamiltonian model. We consider a 2D direct band-gap semiconductor with the Rashba effect dominating at the band edges, affected by the exchange field arising from a magnetic insulator substrate (Fig. 1a). A single-band **k·p** Hamiltonian of this

[1]Department of Physics and Astronomy & Nebraska Center for Materials and Nanoscience, University of Nebraska, Lincoln, NE 68588, USA. ✉email: ltao2@unl.edu ; tsymbal@unl.edu

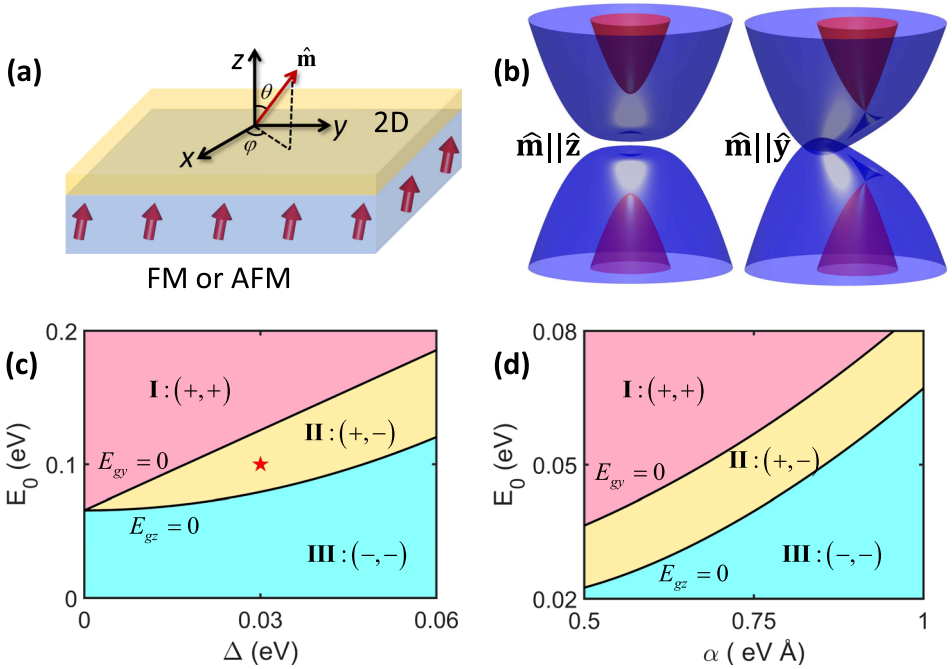

Fig. 1 Phase diagram for Rashba–Zeeman model. a Schematic illustration of the Rashba 2D system on top of a magnetic insulator. Red arrows denote the exchange field whose orientation is determined by the unit vector $\hat{\mathbf{m}} = (sin\theta cos\varphi, sin\theta sin\varphi, cos\theta)$ in spherical coordinates. **b** 3D plot of the calculated band structure with $\hat{\mathbf{m}}$ being parallel to z axis $\hat{\mathbf{m}}||\hat{\mathbf{z}}$ or y axis $\hat{\mathbf{m}}||\hat{\mathbf{y}}$ for $m_c = -m_v = 0.5\, m_0$, $\alpha_c = \alpha_v = 1.0$ eV Å, $E_0 = 0.1$ eV, $\Delta = 0.03$ eV. **c**, **d** Phase diagram in the (E_0, Δ) plane for $\alpha_c = \alpha_v = 1.0$ eV Å. **c** and in the (E_0, α) plane for $\alpha = \alpha_c = \alpha_v$ and $\Delta = 0.01$ eV **d**. The phase boundaries are determined by $E_{gz} = 0$ or $E_{gy} = 0$. The red star in **c** indicates a set of parameters corresponding to the band structure in **b**.

system can be written as follows:

$$H_{c,v} = \frac{\hbar^2 k^2}{2m_{c,v}} + E_{c,v} + \alpha_{c,v}\left(k_x\sigma_y - k_y\sigma_x\right) - \Delta\boldsymbol{\sigma}\cdot\hat{\mathbf{m}}. \quad (1)$$

Here, indices c and v indicate the bottom of the conduction band and the top of the valence band, respectively. The first term represents the kinetic energy with $m_{c,v}$ being the electron effective mass, $E_{c,v}$ is the band edge energy, the third term is the Rashba SOC with $\alpha_{c,v}$ being the Rashba parameters. The last term is the Zeeman term, where $\boldsymbol{\sigma}$ is the Pauli spin matrix, Δ is the exchange field, and the unit vector $\hat{\mathbf{m}}$ denotes the field orientation.

This model realistically describes certain types of 2D materials deposited on a magnetic insulator substrate. Specifically, there exist a handful of 2D direct band-gap semiconductors, such as Ag_2Te[26], BiSb[27], and $LiAlTe_2$[28] monolayers whose electronic structure around the conduction band minimum and the valence band maximum can be well described by the single-band Rashba model. When these monolayers are deposited on a proper magnetic insulator substrate, their electronic structure is expected to be well captured by Eq. (1) provided that the effect of the substrate is dominated by the exchange field. The latter requirement entails a weak electronic hybridization between the 2D material and the substrate, which is expected to be valid for a sufficiently wide band-gap insulator.

Figure 1b shows the calculated electronic structure based on Hamiltonian (1) for typical parameters corresponding to the model. It is seen that the energy spectrum represents four bands (two conduction bands and two valence bands) whose appearance depends on the exchange field orientation. For the exchange field parallel to the z axis ($\hat{\mathbf{m}}||\hat{\mathbf{z}}$), the band gap is opened, whereas for the exchange field parallel to the y axis ($\hat{\mathbf{m}}||\hat{\mathbf{y}}$), the band gap is closed. Thus, by controlling the magnetization direction of the substrate it is possible to achieve a phase transition in the 2D system from the insulating state to the conducting state.

To elucidate this phase transition in more detail, we derive an analytic expression for the band gap. For $\hat{\mathbf{m}}||\hat{\mathbf{z}}$, the band gap E_{gz} is given by (see Supplementary Note 1)

$$E_{gz} = E_0 - \frac{\hbar^2\Delta^2}{2}\left(\frac{1}{m_c\alpha_c^2} - \frac{1}{m_v\alpha_v^2}\right) - \frac{1}{2\hbar^2}\left(m_c\alpha_c^2 - m_v\alpha_v^2\right), \quad (2)$$

where $E_0 = E_c - E_v$ is the band gap in the absence of the Rashba–Zeeman effect. For $\hat{\mathbf{m}}||\hat{\mathbf{y}}$ (or $\hat{\mathbf{m}}||\hat{\mathbf{x}}$), the band gap E_{gy} (or E_{gx}) reads

$$E_{gy} = E_0 - 2\Delta - \frac{1}{2\hbar^2}\left(m_c\alpha_c^2 - m_v\alpha_v^2\right). \quad (3)$$

Note that in Eqs. (2) and (3), the negative sign of the band gap implies band inversion and thus no band gap.

Using Eqs. (2) and (3), we obtain the band gaps E_{gz} and E_{gy} depending on parameters of the model. Figure 1c, d shows the resulting phase diagrams in the (E_0, Δ) and (E_0, α) planes, respectively. It is seen that there are three distinctly different phases I, II, and III classified according to the sign of the band gaps E_{gz} and E_{gy}. The two-phase boundaries (shown by black lines in Fig. 1c, d) are determined by $E_{gz} = 0$ or $E_{gy} = 0$. For phases I and III, both band gaps are positive (phase I) or negative (phase III), indicating the trivial phase transition from insulator-to-insulator (phase I) or from conductor to conductor (phase III). For phase II, we observe a nontrivial insulator-to-conductor transition or via versa as a result of changing the exchange field orientation from the z axis to the $y(x)$ axis. The illustration of this transition is revealed in the band structure of Fig. 1b, which corresponds to a set of parameters indicated by the red star in Fig. 1c.

It is evident that there is a certain range of parameters for which the insulator-to-conductor transition occurs. A smaller E_0 always yields the conductor phase, whereas larger E_0 requires the strong exchange field to induce the insulator-to-conductor transition. A larger Rashba parameter favors the transition for the system with larger E_0. Supplementary Figure 2 shows that the insulator-to-

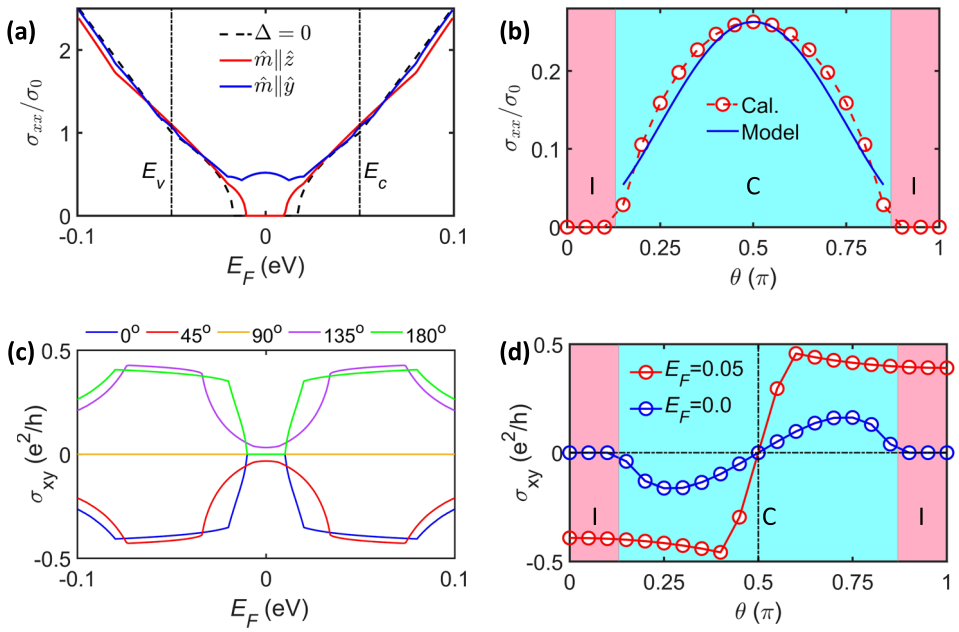

Fig. 2 Electrical conductivity and anomalous Hall conductivity for Rashba–Zeeman model. a Longitudinal conductivity σ_{xx} (in unit of $\sigma_0 = e^2\tau E_R/(\pi\hbar^2)$ as a function of Fermi energy E_F for $\hat{\boldsymbol{m}}\|\hat{\boldsymbol{z}}, \hat{\boldsymbol{m}}\|\hat{\boldsymbol{y}}$ and zero exchange field $\Delta = 0$. **b** σ_{xx} as a function of θ for $E_F = 0$ and $\varphi = 90°$. **c** Anomalous Hall conductivity σ_{xy} as a function of E_F for $\varphi = 90°$ and different θ. **d** σ_{xy} as a function of θ for $E_F = 0$ (magnified five times, blue line) and $E_F = 0.05$ eV (red line) for $\varphi = 90°$. **b**, **d** the rose and aqua colored regions represent the insulating (I) and conducting (C) phases, respectively. The other parameters are fixed as $m_c = -m_v = 0.5\ m_0$, $\alpha_c = \alpha_v = 1.0$ eV Å, $E_0 = 0.1$ eV, $\Delta = 0.03$ eV.

conductor transition is not only limited by equal Rashba parameters α_c and α_v and effective masses m_c and m_v but can also occur for non-equal parameters (see Supplementary Note 2).

Electrical conductivity and anomalous Hall conductivity

The predicted insulator-to-conductor transition can be probed by measuring electrical conductivity. We calculate the conductivity σ_{xx} of the 2D system within the approximation of a constant relaxation time τ, as discussed in Supplemental Note 3. Figure 2a shows σ_{xx} as a function of Fermi energy E_F. In the absence of the exchange field, $\Delta = 0$, σ_{xx} for conduction bands can be expressed analytically as follows (see Supplementary Note 3)

$$\sigma_{xx}/\sigma_0 = \begin{cases} \sqrt{(E_F - E_c)/E_R + 1}, & E_c - E_R < E_F \le E_c \\ (E_F - E_c)/E_R + 1, & E_F > E_c \end{cases}, \quad (4)$$

where $E_R = m_c\alpha_c^2/(2\hbar^2)$ is the Rashba energy and $\sigma_0 = e^2\tau E_R/(\pi\hbar^2)$ is the conductivity unit. This limiting case is shown in Fig. 2a by the dashed line. We see distinct energy dependent behaviors below and above the conduction band minimum. When $\Delta \neq 0$, σ_{xx} depends on the exchange field orientation $\hat{\mathbf{m}}$. It is seen that around $E_F = 0$, the conductivity is zero for $\hat{\mathbf{m}}\|\hat{\mathbf{z}}$ (red line in Fig. 2a), whereas the conductivity is nonzero for $\hat{\mathbf{m}}\|\hat{\mathbf{y}}$ in the whole energy range (blue line in Fig. 2a). For higher Fermi energy, σ_{xx} scales linearly with E_F, as expected from Eq. (4).

Figure 2b shows σ_{xx} as a function of azimuthal angle θ for $\varphi = 90°$ and $E_F = 0$. The critical points for the insulator-conductor transition are around $\theta = 0.13\pi$ and $\theta = 0.87\pi$. In the conducting phase (aqua color), σ_{xx} versus θ can be well described by $\sigma_{xx}(\theta) = \sigma_{xx}(0) + [\sigma_{xx}(\pi/2) - \sigma_{xx}(0)]sin^2\theta$ (blue solid line), which is the conventional behavior known for anisotropic magnetoresistance[29]. Overall, changing the magnetization orientation of the substrate reveals perfect anisotropy in the conductivity of the 2D system.

Probing the anomalous Hall conductivity σ_{xy} provides another way to explore the phase transition. We calculate σ_{xy} assuming that there is only an intrinsic contribution to the anomalous Hall conductivity[30]. This contribution is determined by the Berry curvature as discussed in the Supplemental Note 4. Figure 2c shows the calculated σ_{xy} of the 2D system as a function of E_F for different angles θ (determined in Fig. 1a). It is seen that σ_{xy} is zero in the energy gap region when $\hat{\mathbf{m}}\|\hat{\mathbf{z}}$ ($\theta = 0°$ or $\theta = 180°$). For $\theta = 45°$ or $\theta = 135°$, the gap is closed and σ_{xy} is nonzero in the whole energy range.

Figure 2d shows σ_{xy} as a function of θ changing continuously from 0° to 180°. For $E_F = 0$ (blue circles and line in Fig. 2a), we observe the same critical points for the insulator-conductor transition at around $\theta = 0.13\pi$ and $\theta = 0.87\pi$. This transition disappears for $E_F = 0.05$ eV (red circles and line in Fig. 2d) consistent with Fig. 2c. For any Fermi energy, there is a sign change in σ_{xy} at $\theta = 90°$. This sign change is are explained by the properties of the Berry curvature Ω_z, as demonstrated in Supplementary Fig. 4.

The above approach can be expanded to other types of SOC, such as the Dresselhaus SOC[31] or the Rashba-Dresselhaus SOC[32,33]. The analysis of the 2D systems, which exhibit these types of SOC shows that a similar insulator-to-conductor transition can be observed in both models (see Supplementary Note 5 for details).

DFT results for Ag_2Te/Cr_2O_3

Next, we discuss a possible realization of the insulator-to-conductor transition in a realistic system, namely a monolayer of Ag_2Te deposited on a magnetic Cr_2O_3 (0001) substrate. A buckled Ag_2Te monolayer possesses a 2D hexagonal lattice of the *P6mm* symmetry and has a sizable band gap of 150 meV[26]. Owing to broken inversion symmetry, an Ag_2Te monolayer exhibits Rashba band splitting with a large Rashba parameter of 3.84 eV Å[34] (see Supplementary Note 6 for details). In a non-centrosymmetric corundum structure, Cr_2O_3 is a magnetoelectric AFM insulator which belongs to the magnetic space group is $R\bar{3}'c'$. It exhibits the surface magnetization, which is an intrinsic property of all magnetoelectric antiferromagnets[35,36]. This magnetization is

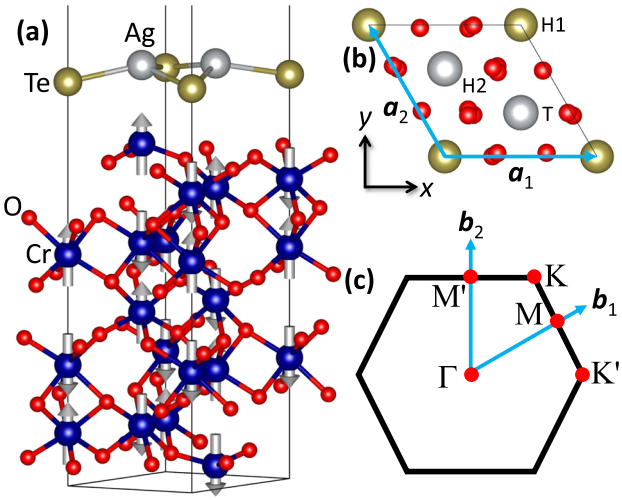

Fig. 3 Atomic structure of the Ag_2Te/Cr_2O_3. a Atomic structure of monolayer Ag_2Te on top of Cr_2O_3(0001) surface. Gray arrows denote the magnetic moments of Cr atoms. **b** Top view of the Ag_2Te/Cr_2O_3 structure. H1/H2 and T represent hollow and top sites, respectively. The black lines denote the unit cell, where the primitive vectors are given by $\boldsymbol{a}_1 = a\hat{\boldsymbol{x}}$, $\boldsymbol{a}_2 = -a/2\hat{\boldsymbol{x}} + \sqrt{3}a/2\hat{\boldsymbol{y}}$. and a is the lattice constant. **d** The Brillouin zone with high-symmetry $\boldsymbol{k}$ points indicated, where the primitive vectors are given by $\boldsymbol{b}_1 = 2\pi/a\boldsymbol{x}\hat{+}2\pi/(\sqrt{3}a)\hat{\boldsymbol{y}}, \boldsymbol{b}_2 = 4\pi/(\sqrt{3}a)\hat{\boldsymbol{y}}$.

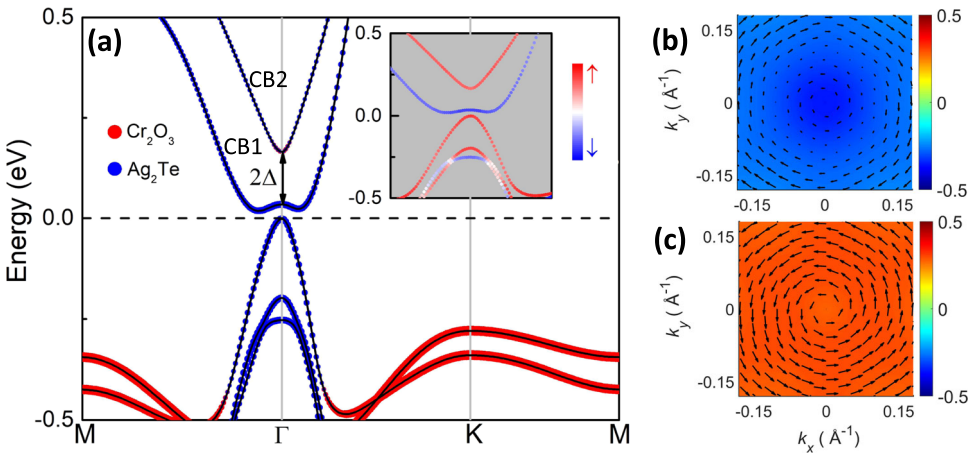

Fig. 4 Band structure and spin textures. a Layer projected band structure of Ag_2Te/Cr_2O_3(0001) for magnetization parallel to z axis. The red and blue circles denote the projection onto the Cr_2O_3 and Ag_2Te layers, respectively. Inset: spin projected band structure with color quantifying the expectation value of s_z component. Spin textures around the Γ point at the bottom two conduction bands denoted by **b** CB1 and **c** CB2. The in-plane spin components s_x and s_y are shown by arrows while the out-of-plane spin component s_z is indicated by color.

electrically switchable with an AFM order parameter of Cr_2O_3, as has been demonstrated in experiment[37]. The exchange coupling between Cr_2O_3 and Ag_2Te across the interface in the Ag_2Te/Cr_2O_3 structure is mediated by the surface magnetization through the proximity effect. The recent work has shown that a topological phase of graphene can be tuned by magnetization orientation in a graphene/Cr_2O_3 system[38].

Figure 3a shows the atomic structure (produced using the VESTA software[39]) of the Ag_2Te/Cr_2O_3(0001) system consisting of monolayer Ag_2Te and Cr_2O_3 substrate composed of 6 and 12 atomic layers of O and Cr, respectively. The magnetic moments of Cr atoms in Cr_2O_3 are aligned parallel in the (0001) plane and antiparallel along the (0001) direction. The Cr_2O_3 surface is terminated by a single layer of Cr, which has the lowest surface energy[40]. As seen from Fig. 3b, the interface atomic configuration has one Te atom and one Ag atom located at the hollow (H) sites and another Ag atom located at the top (T) site of the Cr_2O_3 (0001) surface. This atomic configuration is among three possible highly symmetric atomic structures which have the lowest energy (see Supplementary Note 7).

Figure 4a shows the calculated band structure of Ag_2Te/Cr_2O_3 for magnetization parallel to the z axis. It is noteworthy that the bands near the Fermi energy arise predominantly from the Ag_2Te layer, suggesting weak electronic hybridization between Ag_2Te and Cr_2O_3. Orbital-projected band structure indicates that the bands near the Fermi energy are mainly composed of the Ag-*s*, *d* and Te-*p* orbitals (see Supplementary Note 8), consistent with the previous results[26,34]. A band gap of ~16 meV is observed, and the Zeeman-type spin splitting at the Γ point is $2\Delta = 131$ meV for the bottom of conduction bands. The Rashba-type SOC of the conduction bands is evident from the in-plane spin texture shown in Fig. 4b, c.

Next, we investigate the effect of magnetization orientation on the electronic band structure. Figure 5 shows the calculated

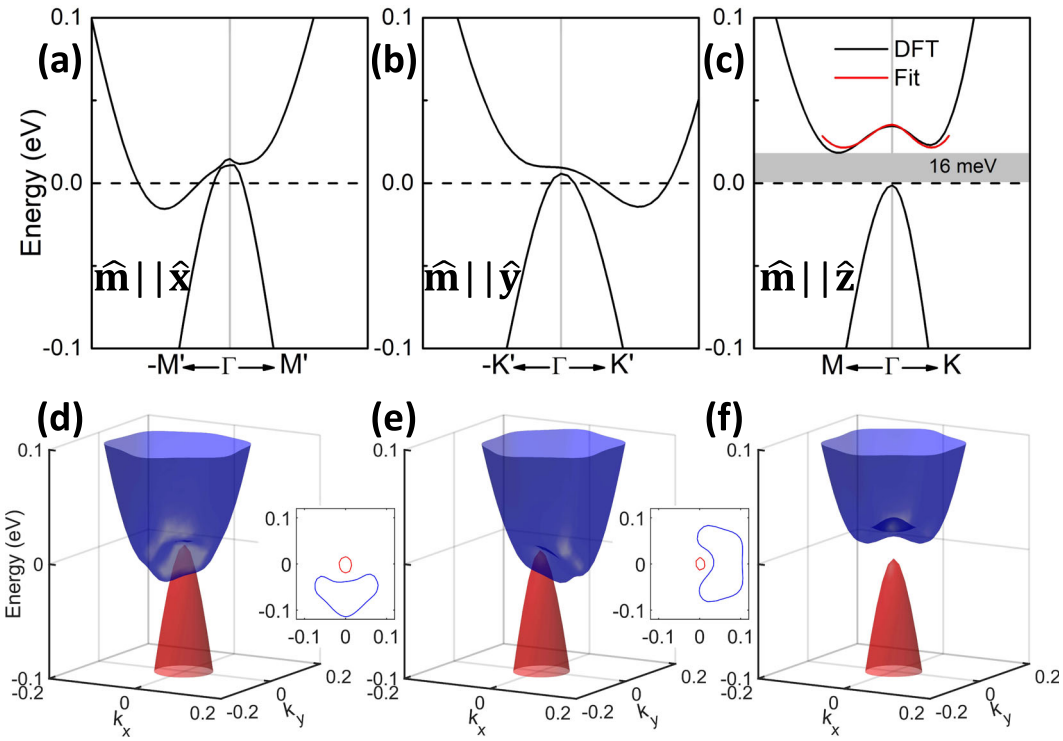

Fig. 5 Magnetization control of band dispersion. Band structure around the Γ point for magnetization parallel to **a**, **d** *x* axis ($\hat{\mathbf{m}}||\hat{\mathbf{x}}$), **b**, **e**. *y* axis ($\hat{\mathbf{m}}||\hat{\mathbf{y}}$), **c**, **f**. *z* axis ($\hat{\mathbf{m}}||\hat{\mathbf{z}}$). **a**–**c** Band dispersion along certain *k* paths. **d**–**f** 3D plot of the band structures around the Γ point. **d**, **e** Fermi contours with the red (blue) line representing the hole (electron) pocket. **c** Fitting to the conduction band around the Γ point is shown by the red line.

results. It is seen that for the in-plane magnetization, i.e., when $\hat{\mathbf{m}}||\hat{\mathbf{x}}$ (Fig. 5a) or $\hat{\mathbf{m}}||\hat{\mathbf{y}}$ (Fig. 5b), the band structure reveals a conducting phase characterized by electron and hole pockets crossing the Fermi energy. In contrast, for the out-of-plane magnetization ($\hat{\mathbf{m}}||\hat{\mathbf{z}}$), a band gap of 16 meV opens and the system is driven into an insulator phase (Fig. 5c). Thus, the Ag_2Te/Cr_2O_3 system can be either a conductor or an insulator depending on the surface magnetization direction of Cr_2O_3 substrate.

We note that in the above calculations, the polarization of Ag_2Te was pointing downward. For polarization pointing upward, the buckling height between Ag and Te layers is suppressed and the bond length between Te and Cr increases, suggesting that the Rashba effect and Zeeman field are both suppressed. The insulator-to-conductor transition does not occur. Also, it is noteworthy that the insulator-to-conductor transition is Cr_2O_3 thickness independent, as expected from the exchange field arising from the magnetic proximity effect at the interface.

Figure 5d–f show 3D plots of the band structure for different magnetization orientations. The Fermi contours, which are shown in insets of Fig. 5d, e, suggest that the hole pocket is nearly a circle centered around the Γ point (red lines), whereas the electron pocket (blue lines) appears in the $k_y < 0$ ($k_x > 0$) quadrant for $\hat{\mathbf{m}}||\hat{\mathbf{x}}$ ($\hat{\mathbf{m}}||\hat{\mathbf{y}}$). This behavior can be well explained by the Rashba–Zeeman model proposed earlier. According to Eq. (1), around the conduction band minimum, the dispersion along the k_y direction for $\hat{\mathbf{m}}||\hat{\mathbf{x}}$ can be expressed as $E_c^- = \hbar^2 k_y^2/2m_c + E_c - \sqrt{(a_c k_y + \Delta)^2}$. Here Δ is negative owing to a higher band energy for spin up than for spin down (inset in Fig. 4a). Thus, we have $E_c^-(k_y<0) < E_c^-(k_y>0)$, indicating that the band energy at $k_y < 0$ is lower than that at $k_y > 0$, which yields the band branch at $k_y < 0$ crossing the Fermi energy. The appearance of the electron pocket at $k_x > 0$ for $\hat{\mathbf{m}}||\hat{\mathbf{y}}$ can be explained in the same way. We note that the shapes of the electron pockets are different for $\hat{\mathbf{m}}||\hat{\mathbf{x}}$ and $\hat{\mathbf{m}}||\hat{\mathbf{y}}$ owing to a higher *k*-order contribution.

Our **k·p** model can be used to describe the DFT calculated band structure of Ag_2Te/Cr_2O_3. Using Supplementary Eq. (1), we fit the conduction band around the Γ point (red line in Fig. 5c). The fitting yields the following Hamiltonian parameters: $m_c = 0.5\ m_0$, $a_c = 1.89$ eV Å, $E_c = 0.03$ eV. According to Supplementary Eqs. (5) and (12), the insulator-to-conductor transition can occur under the condition $E_c < \Delta + m_c a_c^2/2\hbar^2$. This condition is indeed satisfied, which is seen by plugging the fitted parameters into the above inequality.

Experimentally, the predicted insulator-to-conductor transition can be observed in the Ag_2Te/Cr_2O_3 (0001) heterostructure where a 180° AFM domain wall is formed in Cr_2O_3 between two domains with a uniform perpendicular-to-plane Néel vector pointing in opposite directions. In this case, in the domain wall region, the continuous rotation of the surface magnetization in Cr_2O_3 results in the formation of a conducting phase of Ag_2Te, whereas within the domains, Ag_2Te remains insulating (semiconducting). Thus, the enhancement of the electrical conductivity is expected in the domain wall region.

It is noteworthy that the predicted insulator-to-conductor transition in Ag_2Te/Cr_2O_3 may only be observed in the low temperature regime owing to the small band gap of ~16 meV (see Supplementary Note 9). Even though, as seen from Supplementary Fig. 10b, a sizable difference in conductivity between $\hat{\mathbf{m}}||\hat{\mathbf{z}}$ and $\hat{\mathbf{m}}||\hat{\mathbf{y}}$ does exist even at room temperature.

In addition to the Ag_2Te/Cr_2O_3 system, there are other potential candidates with different 2D materials and magnetic substrates to explore the insulator-to-conductor transition. For example, the above mentioned BiSb[27] and $LiAlTe_2$[28] monolayers have a smaller band gap and giant Rashba parameters. The magnetic insulator materials can be extended to FM EuO[41] and CrI_3[42,43], and ferrimagnetic YIG[44]. In comparison with AFM Cr_2O_3, these

magnetic insulators have an advantage of controlling their magnetization by an external magnetic field.

Noteworthy is the fact that the predicted insulator-to-conductor transition is different from the conventional metal–insulator transitions driven by structural distortions, magnetic ordering, and electron correlations via Peierls, Mott, and Slater mechanisms[45]. Within the proposed mechanism, neither the structural distortions nor magnetostructural transitions or electron correlations are essential. The proposed mechanism is also different from the recently predicted insulator-to-conductor transition in van der Waals spin valves[46]. For the latter, gap closing or opening at the Dirac point is due to a change of the on-site potentials via the Zeeman effect and SOC is absent.

In summary, we have predicted the insulator-to-conductor transition that can be triggered by the exchange field via the Rashba–Zeeman, Dresselhaus-Zeeman or Rashba-Dresselhaus-Zeeman effect in 2D/FM or 2D/AFM systems and demonstrated its possible realization for a realistic Ag_2Te/Cr_2O_3 heterostructure using first-principles calculations. We hope that our work will enrich the Rashba–Zeeman physics and stimulate experimental studies of the predicted phenomenon.

METHODS

DFT calculations

Our atomic and electronic structure calculations were performed using the projector-augmented wave method[47,48] implemented in the Vienna ab initio simulation package[49]. An energy cutoff of 400 eV for the plane wave expansion, generalized gradient approximation[50] for the exchange and correlation functional with Hubbard-U correction $U_{\mathrm{eff}} = 2$ eV on Cr-d orbital[51] were adopted throughout. A $4 \times 4 \times 1$ k-point grid for Brillouin zone integration was used for structural relaxation and a $10 \times 10 \times 1$ grid was used for self-consistent electronic structure calculations. The optimized in-plane lattice constant of 4.86 Å for Ag_2Te was found close to the optimized in-plane lattice constant of 4.97 Å (experimental value 4.95 Å[52]) for bulk Cr_2O_3, so that the lattice mismatch was ~2%. We fixed the in-plane lattice constant to be 4.95 Å in all our calculations. The atomic coordinates were fully relaxed in the absence of SOC with the force tolerance of 0.01 V/Å. The DFT-D3 method with Becke–Jonson damping was used to include the van der Waals corrections[53]. A vacuum region of >20 Å along the z direction was imposed in the supercell calculations.

DATA AVAILABILITY

The data that support the findings of this study are available from the corresponding author upon reasonable request.

CODE AVAILABILITY

The related codes are available from the corresponding authors upon reasonable request.

Received: 10 July 2020; Accepted: 15 October 2020;
Published online: 11 November 2020

REFERENCES

1. Rashba, E. Properties of semiconductors with an extremum loop. 1. Cyclotron and combinational resonance in a magnetic field perpendicular to the plane of the loop. *Sov. Phys. Solid State* **2**, 1109–1122 (1960).
2. Manchon, A., Koo, H. C., Nitta, J., Frolov, S. M. & Duine, R. A. New perspectives for Rashba spin-orbit coupling. *Nat. Mater.* **14**, 871–882 (2015).
3. LaShell, S., McDougall, B. A. & Jensen, E. Spin splitting of an Au(111) surface state band observed with angle resolved photoelectron spectroscopy. *Phys. Rev. Lett.* **77**, 3419 (1996).
4. Caviglia, A. D. et al. Tunable Rashba spin-orbit interaction at oxide interfaces. *Phys. Rev. Lett.* **104**, 126803 (2010).
5. Ishizaka, K. et al. Giant Rashba-type spin splitting in bulk BiTeI. *Nat. Mater.* **10**, 521–526 (2011).
6. Di Sante, D., Barone, P., Bertacco, R. & Picozzi, S. Electric control of the giant Rashba effect in bulk GeTe. *Adv. Mater.* **25**, 509–513 (2013).
7. Tao, L. L. & Wang, J. Strain-tunable ferroelectricity and its control of Rashba effect in $KTaO_3$. *J. Appl. Phys.* **120**, 234101 (2016).
8. Datta, S. & Das, B. Electronic analog of the electro-optic modulator. *Appl. Phys. Lett.* **56**, 665 (1990).
9. Tao, L. L. & Tsymbal, E. Y. Two-dimensional spin-valley locking spin valve. *Phys. Rev. B* **100**, 161110(R) (2019).
10. Tao, L. L., Naeemi, A. & Tsymbal, E. Y. Valley-spin logic gates. *Phys. Rev. Appl.* **13**, 054043 (2020).
11. Edelstein, V. M. Spin polarization of conduction electrons induced by electric current in two-dimensional asymmetric electron systems. *Sol. State Commun.* **73**, 233 (1990).
12. Sinova, J. et al. Universal intrinsic spin Hall effect. *Phys. Rev. Lett.* **92**, 126603 (2004).
13. Ivchenko, E. L. & Pikus, G. E. New photogalvanic effect in gyrotropic crystals. *JETP Lett.* **27**, 604 (1978).
14. Ganichev, S. D. Spin-galvanic effect and spin orientation by current in non-magnetic semiconductors. *Int. J. Mod. Phys. B* **22**, 113–114 (2008).
15. Jiang, P., Li, L., Liao, Z., Zhao, Y. X. & Zhong, Z. Spin direction controlled electronic band structure in two dimensional ferromagnetic CrI_3. *Nano Lett.* **18**, 3844–3849 (2018).
16. Cheng, Y., Zhang, Q. & Schwingenschlögl, U. Valley polarization in magnetically doped single-layer transition-metal dichalcogenides. *Phys. Rev. B* **89**, 155429 (2014).
17. Yang, H. X. et al. Proximity effects induced in graphene by magnetic insulators: first-principles calculations on spin filtering and exchange-splitting gaps. *Phys. Rev. Lett.* **110**, 046603 (2013).
18. Xu, L. et al. Large valley splitting in monolayer WS_2 by proximity coupling to an insulating antiferromagnetic substrate. *Phys. Rev. B* **97**, 041405 (2018).
19. Ibrahim, F. et al. Unveiling multiferroic proximity effect in graphene. *2D Mater.* **7**, 015020 (**2020**).
20. Žutić, I., Matos-Abiague, A., Scharf, B., Dery, H. & Belashchenko, K. Proximitized materials. *Mater. Today* **22**, 85–107 (2019).
21. Culcer, D., MacDonald, A. & Niu, Q. Anomalous Hall effect in paramagnetic two-dimensional systems. *Phys. Rev. B* **68**, 045327 (2003).
22. Krempasky, J. et al. Entanglement and manipulation of the magnetic and spin–orbit order in multiferroic Rashba semiconductors. *Nat. Commun.* **7**, 13071 (2016).
23. Krempaský, J. et al. *Operando* imaging of all-electric spin texture manipulation in ferroelectric and multiferroic Rashba semiconductors. *Phys. Rev. X* **8**, 021067 (2018).
24. Yoshimi, R. et al. Current-driven magnetization switching in ferromagnetic bulk Rashba semiconductor (Ge, Mn)Te. *Sci. Adv.* **4**, 9989 (2018).
25. Kammhuber, J. et al. Conductance through a helical state in an Indium antimonide nanowire. *Nat. Commun.* **8**, 478 (2017).
26. Ma, Y., Kou, L., Dai, Y. & Heine, T. Two-dimensional topological insulators in group-11 chalcogenide compounds: M_2Te (M = Cu, Ag). *Phys. Rev. B* **93**, 235451 (2016).
27. Singh, S. & Romero, A. H. Giant tunable Rashba spin splitting in a two-dimensional BiSb monolayer and in BiSb/AlN heterostructures. *Phys. Rev. B* **95**, 165444 (2017).
28. Liu, Z., Sun, Y., Singh, D. J. & Zhang, L. Switchable out-of-plane polarization in 2D $LiAlTe_2$. *Adv. Electron. Mater.* **5**, 1900089 (2019).
29. McGuire, T. & Potter, R. Anisotropic magnetoresistance in ferromagnetic 3d alloys. *IEEE Trans. Magn.* **11**, 1018–1038 (*1975*).
30. Nagaosa, N., Sinova, J., Onoda, S., MacDonald, A. H. & Ong, N. P. Anomalous Hall effect. *Rev. Mod. Phys.* **82**, 1539 (2010).
31. Tao, L. L., Paudel, T. R., Kovalev, A. A. & Tsymbal, E. Y. Reversible spin texture in ferroelectric HfO_2. *Phys. Rev. B* **95**, 245141 (2017).
32. Stroppa, A. et al. Tunable ferroelectric polarization and its interplay with spin–orbit coupling in tin iodide perovskites. *Nat. Commun.* **5**, 5900 (2014).
33. Tao, L. L. & Tsymbal, E. Y. Persistent spin texture enforced by symmetry. *Nat. Commun.* **9**, 2763 (2018).
34. Noor-A-Alam, M., Lee, M., Lee, H. J., Choi, K. & Lee, J. H. Switchable Rashba effect by dipole moment switching in an Ag_2Te monolayer. *J. Phys. Condens. Matter* **30**, 385502 (2018).
35. Andreev, A. F. Macroscopic magnetic fields of antiferromagnets. *JETP Lett.* **63**, 758–762 (1996).
36. Belashchenko, K. D. Equilibrium magnetization at the boundary of a magnetoelectric antiferromagnet. *Phys. Rev. Lett.* **105**, 147204 (2010).
37. He, X. et al. Robust isothermal electric control of exchange bias at room temperature. *Nat. Mater.* **9**, 579–585 (2010).
38. Takenaka, H., Sandhoefner, S., Kovalev, A. A. & Tsymbal, E. Y. Magnetoelectric control of topological phases in graphene. *Phys. Rev. B* **100**, 125156 (2019).
39. Momma, K. & Izumi, F. VESTA 3 for three-dimensional visualization of crystal, volumetric and morphology data. *J. Appl. Crystallogr.* **44**, 1272–1276 (2011).

40. Wysocki, A. L., Shi, S. & Belashchenko, K. D. Microscopic origin of the structural phase transitions at the Cr_2O_3 (0001) surface. *Phys. Rev. B* **86**, 165443 (2012).
41. Lukashev, P. V. et al. Spin filtering with EuO: insight from the complex band structure. *Phys. Rev. B* **85**, 224414 (2012).
42. Huang, B. et al. Layer-dependent ferromagnetism in a van der Waals crystal down to the monolayer limit. *Nature* **546**, 270–273 (2017).
43. Paudel, T. R. & Tsymbal, E. Y. Spin filtering in CrI_3 tunnel junctions. *ACS Appl. Mater. Int.* **11**, 15781–15787 (2019).
44. Cherepanov, V., Kolokolov, I. & Lvov, V. The saga of YIG: Spectra, thermodynamics, interaction and relaxation of magnons in a complex magnons. *Phys. Rep.* **229**, 81–144 (1993).
45. Imada, M., Fujimori, A. & Tokura, Y. Metal-insulator transitions. *Rev. Mod. Phys.* **70**, 1039 (1998).
46. Cardoso, C., Soriano, D., García-Martínez, N. A. & Fernández-Rossier, J. Van der Waals spin valves. *Phys. Rev. Lett.* **121**, 067701 (2018).
47. Blöchl, P. E. Projector augmented-wave method. *Phys. Rev. B* **50**, 17953 (1994).
48. Kresse, G. & Joubert, D. From ultrasoft pseudopotentials to the projector augmented-wave method. *Phys. Rev. B* **59**, 1758 (1999).
49. Kresse, G. & Furthmüller, J. Efficient iterative schemes for ab initio total-energy calculations using a plane-wave basis set. *Phys. Rev. B* **54**, 11169 (1996).
50. Perdew, J. P., Burke, K. & Ernzerhof, M. Generalized gradient approximation made simple. *Phys. Rev. Lett.* **77**, 3865 (1996).
51. Íñiguez, J. First-principles approach to lattice-mediated magneto-electric effects. *Phys. Rev. Lett.* **101**, 117201 (2008).
52. Finger, L. W. & Hazen, R. M. Crystal structure and isothermal compression of Fe_2O_3, Cr_2O_3, and V_2O_3 to 50 kbars. *J. Appl. Phys.* **51**, 5362 (1980).
53. Grimme, S., Ehrlich, S. & Goerigk, L. Effect of the damping function in dispersion corrected density functional theory. *J. Comp. Chem.* **32**, 1456 (2011).

ACKNOWLEDGEMENTS

This research was supported by the National Science Foundation through the E2CDA program (grant ECCS-1740136) and the Semiconductor Research Corporation (SRC) through the nCORE program. Computations were performed at the University of Nebraska Holland Computing Center.

AUTHOR CONTRIBUTIONS

L.L.T. and E.Y.T. conceived the project. L.L.T. carried out numerical calculations. Both authors discussed the results and wrote the manuscript.

COMPETING INTERESTS

The authors declare no competing interests.

ADDITIONAL INFORMATION

Supplementary information is available for this paper at https://doi.org/10.1038/s41524-020-00441-0.

Correspondence and requests for materials should be addressed to L.T. or E.Y.T.

Reprints and permission information is available at http://www.nature.com/reprints

Publisher's note Springer Nature remains neutral with regard to jurisdictional claims in published maps and institutional affiliations.

Open Access This article is licensed under a Creative Commons Attribution 4.0 International License, which permits use, sharing, adaptation, distribution and reproduction in any medium or format, as long as you give appropriate credit to the original author(s) and the source, provide a link to the Creative Commons license, and indicate if changes were made. The images or other third party material in this article are included in the article's Creative Commons license, unless indicated otherwise in a credit line to the material. If material is not included in the article's Creative Commons license and your intended use is not permitted by statutory regulation or exceeds the permitted use, you will need to obtain permission directly from the copyright holder. To view a copy of this license, visit http://creativecommons.org/licenses/by/4.0/.

© The Author(s) 2020